




Article

Degradation of Methylene Blue Dye in the Presence of Visible Light Using $\text{SiO}_2@ \alpha\text{-Fe}_2\text{O}_3$ Nanocomposites Deposited on SnS_2 Flowers

Sridharan Balu ¹ , Kasimayan Uma ^{2,*}, Guan-Ting Pan ¹ , Thomas C.-K. Yang ^{1,2,*}  and Sayee Kannan Ramaraj ³

¹ Department of Chemical Engineering and biotechnology, National Taipei University of Technology, Taipei 106, Taiwan, bsridharanbsc.12@gmail.com (S.B.); t6679013@gmail.com (G.-T.P.)

² Precision Analysis and Research Center, National Taipei University of Technology, Taipei 106, Taiwan

³ PG & Research Department of Chemistry, Thiagarajar College, Madurai 625009, Tamilnadu, India; sayeekannanramaraj@gmail.com

* Correspondence: umamahesh16@gmail.com (K.U.); ckyang@mail.ntut.edu.tw (T.C.-K.Y.)

Received: 3 April 2018; Accepted: 13 June 2018; Published: 17 June 2018



Abstract: Semiconductor materials have been shown to have good photocatalytic behavior and can be utilized for the photodegradation of organic pollutants. In this work, three-dimensional flower-like SnS_2 (tin sulfide) was synthesized by a facile hydrothermal method. Core-shell structured $\text{SiO}_2@ \alpha\text{-Fe}_2\text{O}_3$ nanocomposites were then deposited on the top of the SnS_2 flowers. The as-synthesized nanocomposites were characterized by X-ray diffraction (XRD), Raman spectroscopy, field emission scanning electron microscopy (FE-SEM), transmission electron microscopy (TEM), X-ray photoelectron spectroscopy (XPS), UV-Vis Spectroscopy, Brunauer-Emmett-Teller (BET) surface area analysis, and photoluminescence (PL) spectroscopy. The photocatalytic behavior of the $\text{SnS}_2\text{-SiO}_2@ \alpha\text{-Fe}_2\text{O}_3$ nanocomposites was investigated by observing the degradation of methylene blue (MB). The results show an effective enhancement of photocatalytic activity for the degradation of MB especially for the 15 wt % $\text{SiO}_2@ \alpha\text{-Fe}_2\text{O}_3$ nanocomposites on SnS_2 flowers.

Keywords: photocatalyst; flower-like SnS_2 ; nanocomposites; visible light; methylene blue

1. Introduction

Environmental pollution is largely caused by the willful disposal of waste and toxic pollutants without proper treatment. Increasingly, this leads to soil and water degradation, which is deleterious to human health [1,2]. In order to rectify this problem, a variety of processes have been adopted to remove pollutants from wastewater, including adsorption [3], oxidation [4], reduction, and flocculation [5]. Among these various methods, photocatalysis has shown good potential for the removal of organic pollutants [6–8]. It has been reported that a number of semiconductors can be used to degrade a variety of organic pollutants using irradiation of light with different wavelengths [9,10]. When compared with other organic compounds, dyes are the most tested substrates in photocatalytic degradation under solar light, because dyes are considered as the common industrial pollutants, and their concentrations can be easily monitored using a UV-Vis spectrometer. However, the dyes also absorb light, especially in the visible range, the influence of this photo absorption by dyes should be excluded from the evaluation of the real photocatalytic activity of photocatalysts. Among the various dyes, methylene blue (MB) is a heterocyclic aromatic compound, which is poisonous and highly dangerous and causes breathing hazards, vomiting, hyperhidrosis, and mental disorders [11,12]. Many researchers have

focused on thiazine dyes with a dominance of methylene blue, and 37% of published papers reported on the photodegradation of MB dye [13,14].

There are several semiconductor materials that have been used for the promotion of photocatalytic activity. Among these, ecofriendly iron oxide (α -Fe₂O₃) nanomaterials exhibit favorable photocatalytic activity [15] due to their high specific surface area and high crystallinity, and they have the additional advantage of being low cost [16,17]. Hematite (α -Fe₂O₃) is the most stable iron oxide under ambient conditions, and due to its narrow band gap, it can act as a visible light photocatalyst [18]. This makes α -Fe₂O₃ a good potential candidate for a photocatalyst, yielding an enhancement of quantum efficiency when irradiated by visible light [9]. Nowadays, many researchers have tried to improve the photocatalytic behavior of Fe₂O₃ by coupling it with different semiconductor metal oxide nanoparticles, nanotubes, and nanoflowers [19,20]. Metal sulfide semiconductors [21], such as SnS₂, usually have high light absorption qualities in the visible and shorter wavelengths near the infrared (IR) regions [22]. SnS₂ has also been used as an n-type semiconductor due to its low band gap value of 2.2 eV [23]. Tin sulfide is also widely used as an energy material due to its simple binary composition and the abundance of tin and sulfur [24,25]. It is often used in research because of its unique physicochemical properties with low toxicity and good chemical stability and because it is inexpensive [26]. In addition, with its unique multilayer flower-like structure, SnS₂ exhibits superior photocatalytic degradation of MB under visible light [27].

In this research, SiO₂ nanoshells were used to maintain the structure of the nanocomposites and also to avert their aggregation during photocatalytic reactions [28,29]. This is very important in order to ensure the imperishability of the photocatalyst [30]. The preference of SiO₂ for the inner core is based on the following two considerations: First, the silica nanospheres can produce multiple reflections of the visible light irradiated into the internal cavity [31]; second, the well-ordered and smooth structure of SiO₂ promotes the adsorption of dye molecules to the semiconductor material [32,33]. Also, the SiO₂ nanospheres are possessing large active sites that enable easy access of pollutants and, consequently, to improve the catalytic activity when the TiO₂ and Fe₂O₃ nanoparticles are deposited on the SiO₂ nanospheres [34–36].

We report a simplified approach for the synthesis of SnS₂-SiO₂@ α -Fe₂O₃ nanocomposites by means of the hydrothermal method. The photocatalytic activity of the SnS₂-SiO₂@ α -Fe₂O₃ nanocomposites was examined for the degradation of MB under irradiation by visible light. Additionally, samples with different weight percentages of SiO₂@ α -Fe₂O₃ on the SnS₂ flowers were studied to find the optimal ratio for the best photocatalytic activity.

2. Experimental Procedure

2.1. Materials Used

Tin (IV) chloride pentahydrate (98%, Sigma Aldrich, St. Louis, MO, USA), Thioacetamide (TAA 99%, Acros, NJ, USA), Isopropyl Alcohol (Tedia, Fairfield, CT, USA), Ethanol (99%, Fisher Chemicals, NH, USA), tetraethylorthosilicate (TEOS 95%, Acros, NJ, USA), ammonia solution (Choneye Pure Chemicals, Miaoli, Taiwan), iron (III) chloride hexahydrate (97%, Sigma Aldrich, St. Louis, MO, USA), and MB were used. All the above reagents were analytical grade without any additional purification. Deionized water was used throughout the reaction and synthesis process.

2.2. Synthesis of Flower-Like SnS₂

SnS₂ flowers were prepared through a facile hydrothermal method using the same procedure as reported previously [37]. In brief, the procedure for the synthesis of the SnS₂ flowers is as follows: 0.45 g SnCl₄·5H₂O and 0.33 g thioacetamide (TAA) were dissolved in 30 mL isopropyl alcohol. After 30 min of vigorous stirring, the solution was transferred to a Teflon-lined stainless-steel autoclave with a volume of 50 mL and then transferred to a muffle furnace where a hydrothermal was applied

treatment at 180 °C for 24 h. The golden colored precipitates were then centrifuged and rinsed with copious amounts of deionized water and ethanol before being dried in a vacuum for 12 h at 80 °C.

2.3. Synthesis of $\text{SiO}_2@ \alpha\text{-Fe}_2\text{O}_3$ Composite Spheres

In this experiment, silica spheres were synthesized using the same procedure described in our previous work [38]. A mixture of tetraethyl orthosilicate (TEOS) (5 mL), anhydrous ethanol (25 mL), and (5 mL) water was stirred at room temperature for 30 min, followed by the addition of 1 mL of ammonia solution. Next, 15 mL of anhydrous ethanol was added to the above mixture, which was stirred for 12 h at room temperature. After centrifugation, the SiO_2 was collected and washed several times with water and ethanol. Finally, the obtained SiO_2 spheres were dried in a vacuum oven at 60 °C for 12 h. Using ultrasonication, 100 mg of SiO_2 spheres were uniformly dispersed in 40 mL of water, followed by the addition of 50 mg iron (III) chloride hexahydrate and 30 mg urea. The mixture was continuously stirred at 95 °C for 6 h. The FeOOH -coated SiO_2 spheres were separated by centrifugation and then washed several times with water and ethanol. Finally, the spheres were dried in a vacuum oven at 60 °C for 12 h. The resulting FeOOH -coated SiO_2 composite spheres were calcined at 450 °C for 4 h to get crystalline $\alpha\text{-Fe}_3\text{O}_4$ nanoparticles.

2.4. Preparation of $\text{SnS}_2\text{-SiO}_2@ \alpha\text{-Fe}_2\text{O}_3$ Nanocomposites

The $\text{SnS}_2\text{-SiO}_2@ \alpha\text{-Fe}_2\text{O}_3$ (SSF) nanocomposites were prepared by adding 100 mg of flower-like SnS_2 and different weight ratios (5, 10, 15, 20, 25 mg) of $\text{SiO}_2@ \alpha\text{-Fe}_2\text{O}_3$ nanocomposites at 70 °C followed by effective stirring for 5 h. The resultant product obtained by centrifugation was then washed with ethanol and water. The obtained products were labeled $\text{SSF-X} = 5, 10, 15, 20, 25$ wt % corresponding to the weight ratio of the $\text{SiO}_2@ \alpha\text{-Fe}_2\text{O}_3$ nanocomposites.

2.5. Degradation of MB Dye

The as-synthesized $\text{SnS}_2\text{-SiO}_2@ \alpha\text{-Fe}_2\text{O}_3$ (SSF-15 wt %) nanocomposites (40 mg) were dispersed in 100 mL of 5 ppm MB dye solution and stirred at 30 min in the dark. The reaction dye solution was then irradiated under visible light. A 410 nm LED light (Shenzhen Run lite Tech., Shenzhen, China; T2835-0.06W, 12V DC) was placed on the top of the sample bottle used as a visible light source. A 5 mL sample was taken every 15 min, and the degradation was monitored by using UV–Vis spectroscopy. The proceeding degradation of MB obtained by using $\alpha\text{-Fe}_2\text{O}_3$, SnS_2 , and $\text{SiO}_2@ \alpha\text{-Fe}_2\text{O}_3$ were observed to check on the photocatalytic activity.

2.6. Characterization

The X-Ray diffraction studies were carried out using the $\text{Cu-K}\alpha$ line XRD (PANalytical X'Pert PRO, Almelo, Netherlands), The FTIR experiment was carried out using (PerkinElmer Frontier FT-IR Spectrometer, Seer Green, UK) in the range between 400 and 4000 cm^{-1} . The structure and morphology of the catalysts were analyzed using a field emission scanning electron microscopy (FE-SEM) (JEOL, JSM-7610F, Tokyo, Japan). The transmission electron microscopy (TEM) was carried out using (JEOL, JEM2100F, Peabody, MA, USA). The UV–Vis diffused reflectance spectra (DRS) were taken using an (Agilent Technology, Cary5000, Santa Clara, CA, USA). The surface area of the as-synthesized nanocomposites was obtained by Brunauer–Emmett–Teller (BET), using a (Micromeritics–Gemini V, ASAP 2020, Norcross, GA, USA). Photoluminescence (PL) studies were carried out using a (Dongwoo-Ramboss 500i, PL Spectrometer, Gyeonggi-Do, Korea). The X-ray photoelectron (XPS) spectroscopy was analyzed using a (JEOL, JPS-9030, Tokyo, Japan). The electrochemical impedance spectroscopy (EIS) was carried out using a Zive Potentiostat (SP100, eDAQ Inc., Colorado Springs, CO, USA).

3. Results and Discuss

3.1. X-Ray Diffraction

The crystalline nature of the obtained samples was confirmed by XRD. The XRD results for the as-prepared SnS₂ and SnS₂-SiO₂@ α -Fe₂O₃ (SSF-X) (X = 5, 10, 15, 20, and 25 wt %) are shown in Figure 1. The inset to the figure shows the set of peaks at 28.29°, 32.2°, 41.8°, 50.1°, 52.5°, and 55.2°, which can be indexed to the pure hexagonal phase of SnS₂, as confirmed by JCPDS 75-0367 [39]. A peak at 23° confirms the amorphous SiO₂, and the peak appearance at 33° and 35.8° corresponds to α -Fe₂O₃ in Figure S1. After the addition of various concentrations of SiO₂@ α -Fe₂O₃ to the SnS₂ flowers, the intensity of the SnS₂ decreased due to the deposition of the SiO₂@ α -Fe₂O₃ nanocomposites. Figure 1 clearly shows the 2 θ peak at 32.2°, which corresponds to the (011) diffraction planes indexed to the (011) crystalline SnS₂, which in turn decreased with an increase in the concentration of the SiO₂@ α -Fe₂O₃ nanocomposites on SnS₂, confirming the deposition of SiO₂@ α -Fe₂O₃ nanocomposites.

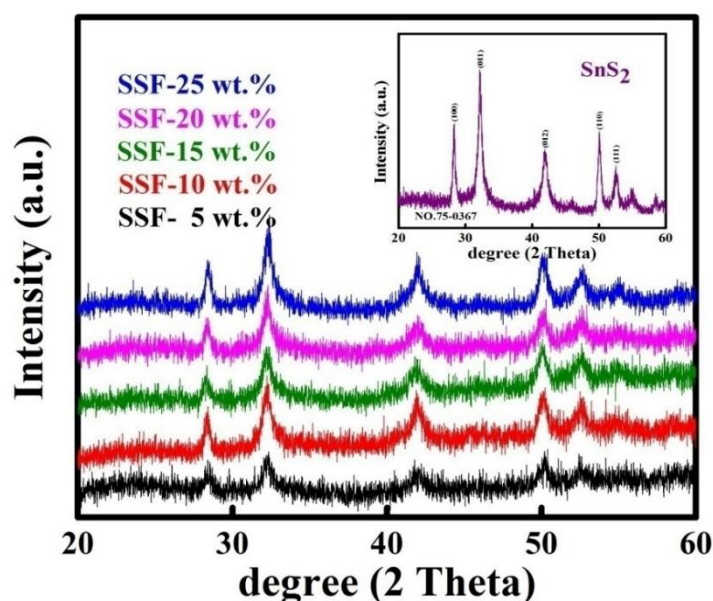


Figure 1. XRD patterns for SnS₂-SiO₂@ α -Fe₂O₃ nanocomposites with different concentrations (SSF-5, 10, 15, 20, and 25 wt %). The inset shows the XRD pattern for as-synthesized flower-like SnS₂.

3.2. FE-SEM Structure

The structural morphologies of SnS₂, α -Fe₂O₃, and SnS₂-SiO₂@ α -Fe₂O₃ were studied using FE-SEM. The flower-like morphology of the as-prepared SnS₂ can be clearly observed in the FE-SEM images. This morphology is produced by the accumulation of several nanosheets assembled at one solitary point. Interestingly, the uniform nanosheet morphology is primarily caused by the intrinsic anisotropic growth of SnS₂ crystals [37]. The size of each nanosheet is about 20 nm, and the size of the full flower-like structure is in a range between 3 and 4 μ m, as shown in Figure 2a. In the SnS₂-SiO₂@ α -Fe₂O₃ composites, α -Fe₂O₃ nanoparticles are deposited on the surface of SiO₂ spheres with a size of around 150 nm, as shown in Figure 2b. The SiO₂@ α -Fe₂O₃ nanocomposites rest on the surface of the SnS₂ flowers, as shown in Figure 2c. The SiO₂ core-shell structure allows the multiple reflections of visible light, and the α -Fe₂O₃ and SnS₂ are used to enhance the absorbance sites. An energy dispersive X-ray Analysis (EDX) observations confirmed the presence of SnS₂-SiO₂@ α -Fe₂O₃ composites. The EDX results give energy peaks congruent with the elements of Sn, S, Fe, O, and Si in Figure 2d.

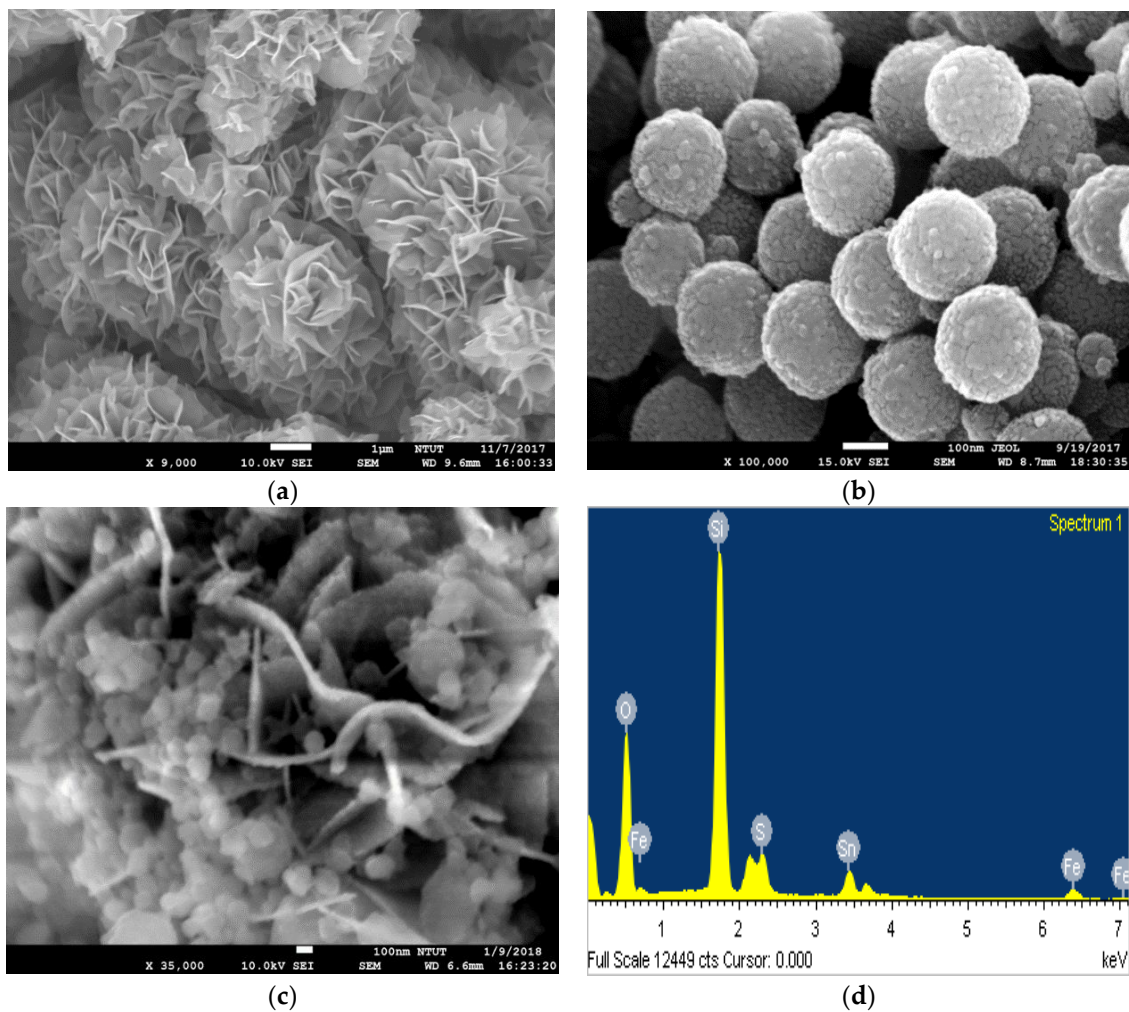


Figure 2. FE-SEM images of (a) Flower-like SnS_2 , (b) $\text{SiO}_2@ \alpha\text{-Fe}_2\text{O}_3$ nanocomposites, (c) $\text{SnS}_2\text{-SiO}_2@ \alpha\text{-Fe}_2\text{O}_3$ nanocomposite, and (d) EDX spectra corresponding to a $\text{SnS}_2\text{-SiO}_2@ \alpha\text{-Fe}_2\text{O}_3$ nanocomposite.

3.3. TEM

The detailed structural and morphological properties of as-prepared SnS_2 and nanocomposites were examined by transmission electron microscopy (TEM). Figure 3 shows the TEM images of as-synthesized flower-like SnS_2 (a). The $\text{SiO}_2@ \alpha\text{-Fe}_2\text{O}_3$ nanospheres are arranged on the surface of SnS_2 flowers (b). This clearly indicates that the $\text{SiO}_2@ \alpha\text{-Fe}_2\text{O}_3$ nanocomposites are observed on the SnS_2 flower, still maintains the flower like structure.

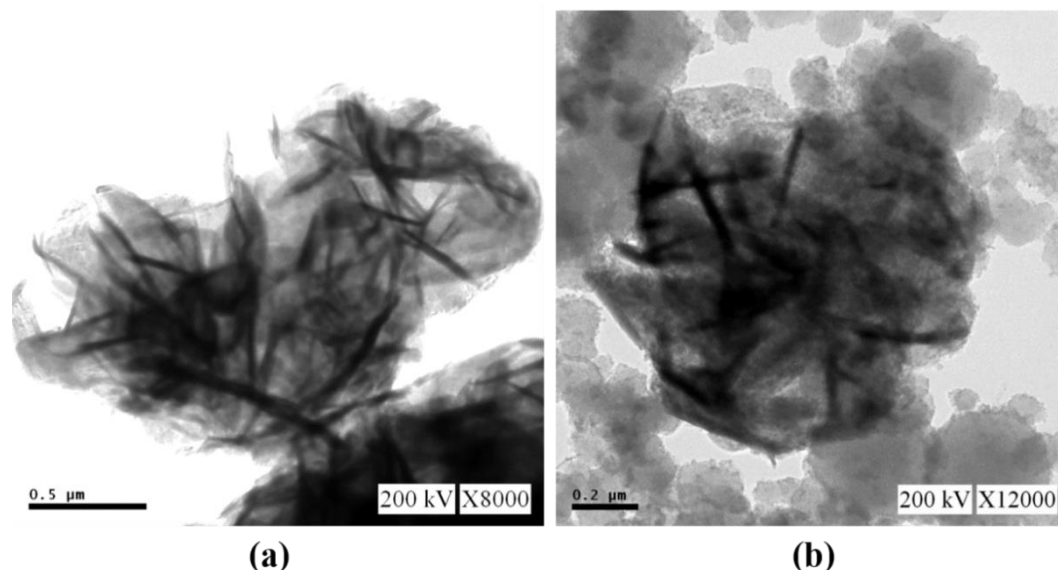


Figure 3. TEM images of (a) Flower-like SnS₂, (b) SnS₂-SiO₂@ α -Fe₂O₃ nanocomposite.

3.4. XPS

To further confirm the elements, their composition, chemical bonding, and oxidation state of the materials, we used X-ray photoelectron spectroscopy (XPS). Figure 4a is the XPS survey spectrum of SnS₂-SiO₂@ α -Fe₂O₃ (SSF-15 wt %) nanocomposite. This demonstrates that the corresponding signals of the main elements Sn, S, Si, O, and Fe were present in the composite. Figure 4b–f shows the high-resolution XPS spectra of Sn 3d, S 2p, O 1s, Fe 2p, and Si 2p. In Figure 4b, the distinctive peaks at 496.7 and 488 eV correspond to the binding energies of Sn 3d_{5/2} and Sn 3d_{3/2}, respectively, indicating the Sn⁴⁺ oxidation state of Sn [40]. Figure 4c shows the enlarged XPS spectrum of S-contained peaks at 161.2 and 163.4 eV, ascribed to the binding energies of S 2p_{3/2} and S 2p_{1/2}, showing the presence of S in S²⁻ state [41]. In the high-resolution XPS spectrum of O in Figure 4d, the typical peaks at 531.6 and 533.4 could be assigned to O 1s having O in O²⁻ state [42]. Figure 4e shows the narrow-scan XPS spectrum of Fe 2p having binding energies at 711.3, 715.9, and 718.3 eV, assigned to the Fe 2p_{3/2}, satellite peak and Fe 2p_{1/2}, respectively [43,44]. The peaks at binding energy 103.6 and 105.1 eV correspond to Si 2p_{3/2} and Si 2p_{1/2} of Si⁴⁺ in SiO₂ [45]. From the XPS results, the successful formation of a SnS₂-SiO₂@ α -Fe₂O₃ nanocomposite can be proved by the binding energies of each element.

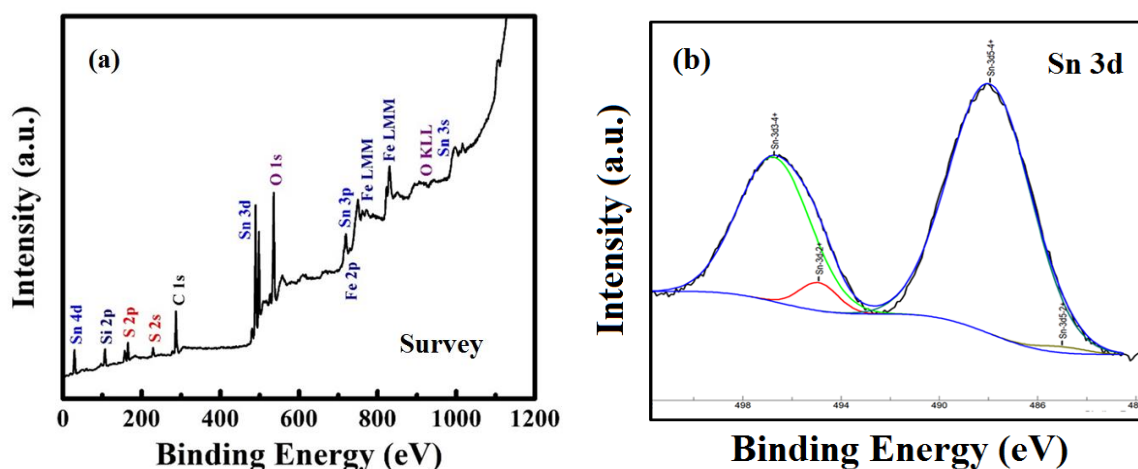


Figure 4. Cont.

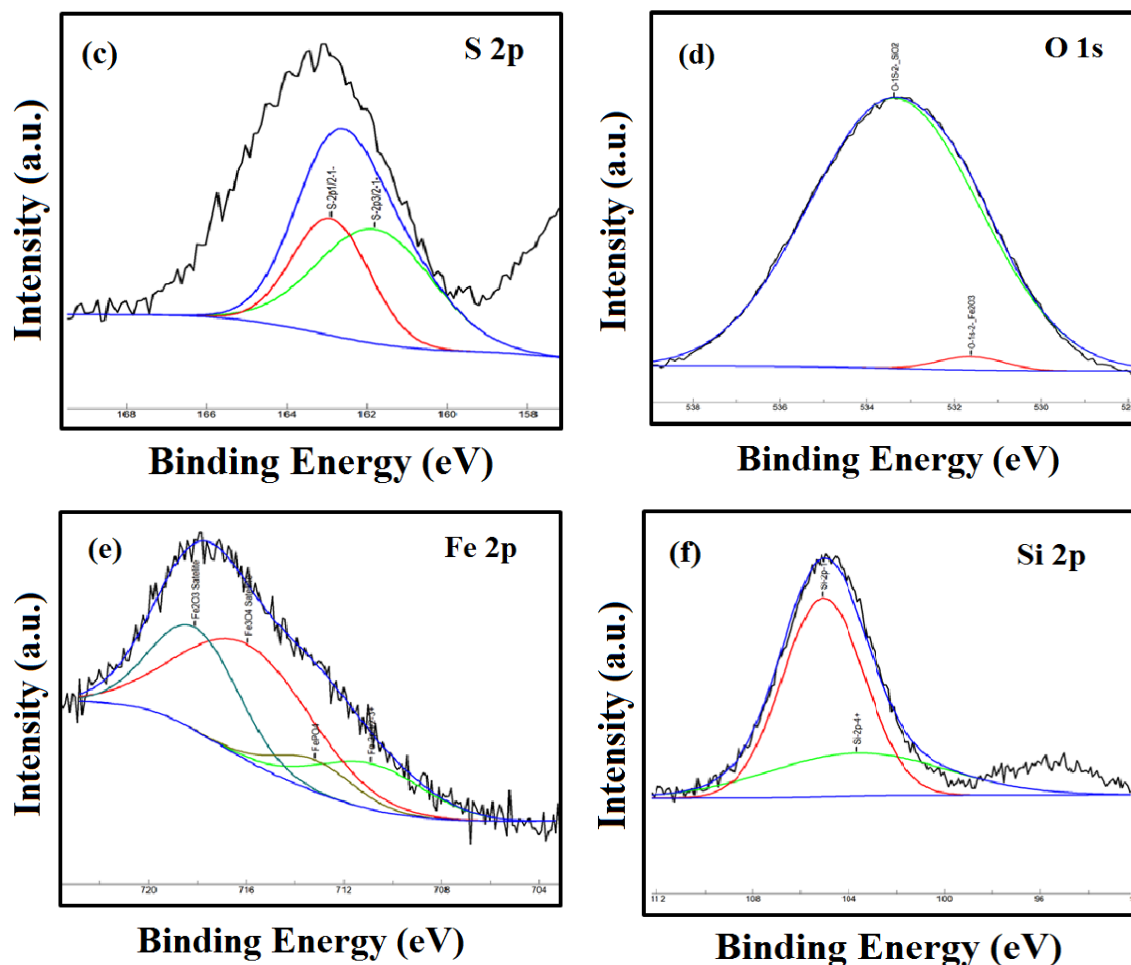


Figure 4. XPS (a) survey spectrum of SSF-15 wt % nanocomposite (b–f) Sn 3d, S 2p, O 1s, Fe 2p, and Si 2p.

3.5. EIS Spectra

The EIS spectra were obtained for the different SnS₂-SiO₂@ α -Fe₂O₃ (SSF-X) (X = 5, 10, 15, 20, and 25 wt %) nanocomposite samples with a modified glassy carbon electrode (GCE) for the KCl (0.1 M) containing 5 mM of [Fe(CN)₆]³⁻ and [Fe(CN)₆]⁴⁻. This EIS spectrum shows the electrical and interfacial properties of the aforementioned nanocomposite materials. The SSF-15 wt % nanocomposite produces a smaller semi-circle in comparison to the other composites. In Figure 5, the smallest semi-circle, with a reduced diameter, indicates very low resistance. The electron transfer resistance observed is 154, 149, 150, 145, and 101 k Ω^{-1} for the various 25, 20, 15, 10, and 5 wt % composites, respectively. The low resistance observed for the SSF-15 wt % nanocomposite is due to the counterpart (stoichiometric) ratio between SnS₂ and SiO₂@ α -Fe₂O₃. The deposition of SiO₂@ α -Fe₂O₃ on the SnS₂ flowers plays an important role in enhancing the charge resistance, due to the low specific capacity of the nanocomposites. This increased electrical conductivity can also extend the lifespan of the charge carriers, as well as increase the reduction in the electron–hole recombination rate. It is also worth noting that higher impedance values were observed for the 15 wt % of SiO₂@ α -Fe₂O₃ nanocomposites, as opposed to all of the other nanocomposites.

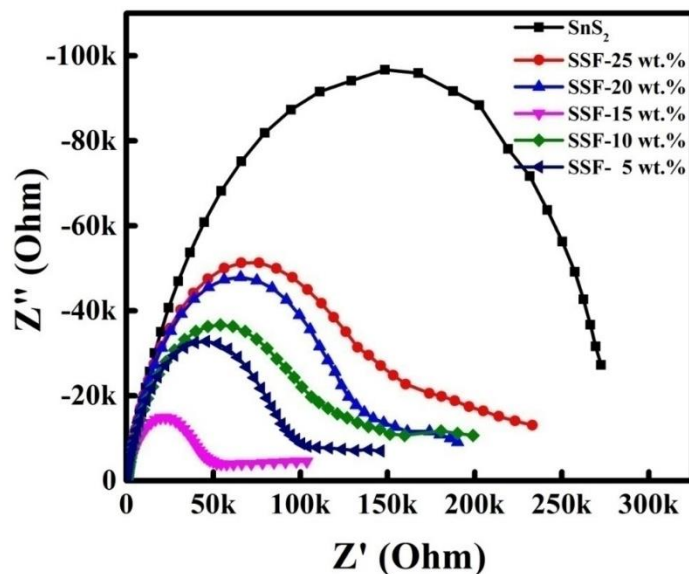


Figure 5. Electrochemical impedance spectroscopy (EIS) spectra of SnS_2 and different concentrations of SSF-X nanocomposites ($X = 5, 10, 15, 20,$ and 25 wt %).

3.6. UV-Vis DRS Spectra

The broad optical absorption capabilities in the entire visible light spectrum in Figure 6, which is commonly defined in the wavelength range of 400–700 nm, imply that all composites are efficient visible light-sensitive photocatalysts. The SSF-15 wt % indicates that composites have strong and broader absorption in the visible light region, suggesting their potential capabilities effectively utilize visible light energy. This can be attributed to the synergetic effect between SnS_2 and $\alpha\text{-Fe}_2\text{O}_3$ nanocomposites. Consequently, the composition SSF-15 wt % enhanced the absorption in the visible light region, which may lead to a higher photocatalytic activity when compared with other weight percentage compositions.

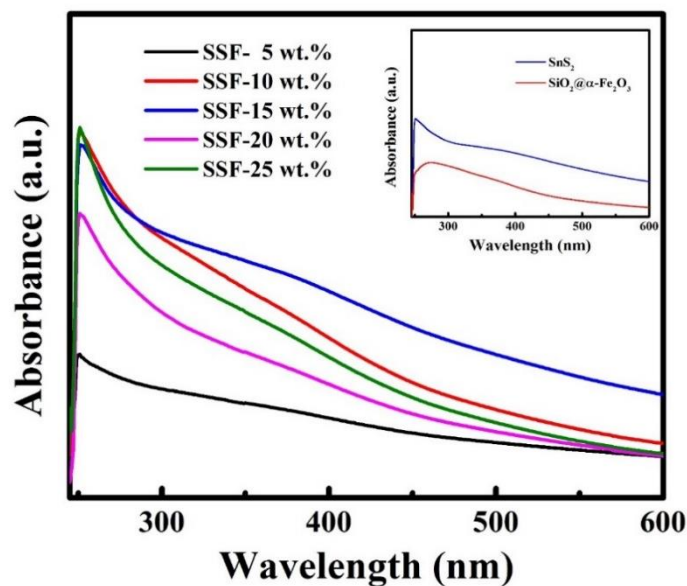


Figure 6. UV-Visible diffused reflectance spectra (DRS) spectra of as-synthesized SSF-X ($X = 5, 10, 15, 20, 25$ wt %); the inset shows DRS spectra of SnS_2 and $\text{SiO}_2@ \alpha\text{-Fe}_2\text{O}_3$.

3.7. FTIR Spectra

The FTIR spectra of the SnS₂ flowers, SiO₂ spheres, and α-Fe₂O₃ and SnS₂-SiO₂@α-Fe₂O₃ nanocomposites are shown in Figure 7. The inset to the figure shows the distinctive peaks at 1535 cm⁻¹ and 1657 cm⁻¹ representative of the SnS₂. A strong stretching vibration of Si-O-Si at 1111 cm⁻¹, a symmetric vibration of the Si-O-Si at 800 cm⁻¹, and a symmetric stretching vibration of the Si-OH bond at 956 cm⁻¹ and 3246 cm⁻¹ can be observed. An absorption peak in the range between 3245 and 3450 cm⁻¹ appears for all the samples after they have been annealed at 450 °C due to the stretching vibration of the OH band, which indicates the presence of the -OH group [38]. As the percentage of SiO₂@α-Fe₂O₃ increases from low to high, there is not much variation in the FTIR spectra. However, the stretching vibrations, which are observed for all the samples, confirm the presence of OH groups. The bands observed at 474 cm⁻¹ and 572 cm⁻¹ are due to the Fe-O metal oxide stretching vibration modes, while the peak at 1052 cm⁻¹ indicates the presence of the Fe-OH group.

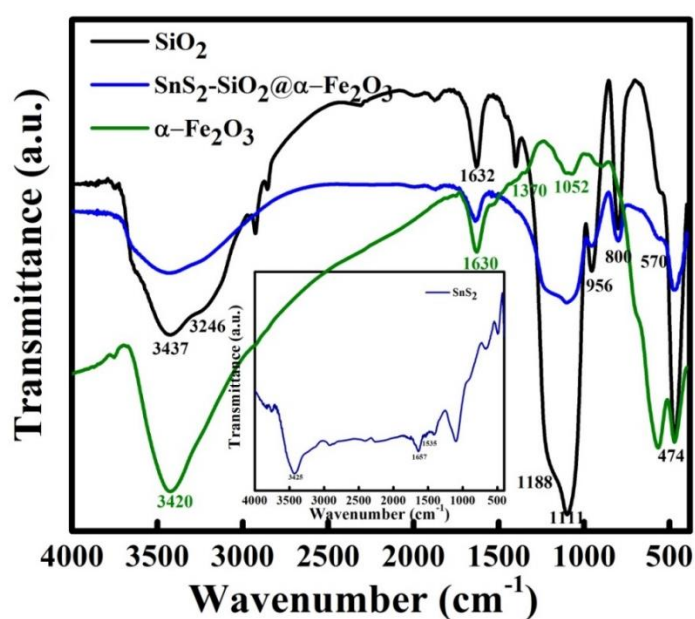


Figure 7. FTIR spectra of SiO₂, α-Fe₂O₃, and SnS₂-SiO₂@α-Fe₂O₃ composites; inset shows the SnS₂ spectra.

3.8. Raman Spectroscopy

Figure 8 shows the Raman spectra for the SnS₂-SiO₂@α-Fe₂O₃ (SSF-X) (X = 5, 10, 15, 20, and 25 wt %) nanocomposites observed in the range of 100 to 1000 cm⁻¹. The Raman spectrum for SnS₂ exhibits an intense peak at about 315 cm⁻¹, which is attributed to the A_{1g} mode [46,47] (Figure 8 [inset]). Increasing the concentration of SiO₂@α-Fe₂O₃ produces no change in the SnS₂ flower-like structure, as shown in Figure 8. For comparison, the Raman spectra of SiO₂ and SiO₂@α-Fe₂O₃ are shown in Figure S2.

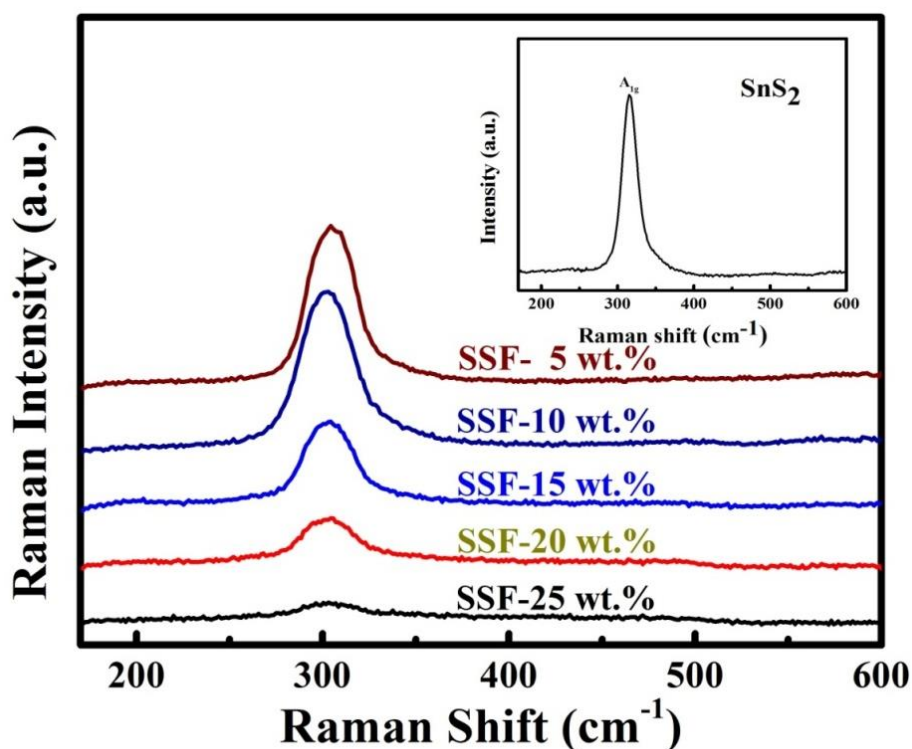


Figure 8. Raman spectra of SnS₂-SiO₂@ α -Fe₂O₃ nanocomposites with various concentrations (SSF-5, 10, 15, 20, and 25 wt %); inset shows the Raman spectra of flower-like SnS₂.

3.9. BET Surface

The surface areas of the as-synthesized SnS₂-SiO₂@ α -Fe₂O₃ (SSF-X) (X = 5, 10, 15, 20, and 25 wt %) composites are characterized by nitrogen adsorption-desorption Brunauer–Emmett–Teller (BET) analysis, as shown in Table 1. From the results of BET analysis, the specific surface areas of SSF-X (X = 5, 10, 15, 20, and 25 wt %) are calculated to be 41.61, 39.41, 42.8, 41.93, and 40.47 m²/g, respectively. From the above results, it can be seen that the surface area of SSF-15 is slightly higher among all specimens. This implies that the enhancement of the adsorption capacity occurred in SSF-15, compared to that of the plain SnS₂ flowers.

Table 1. Brunauer–Emmett–Teller (BET) surface areas of various SnS₂-SiO₂@ α -Fe₂O₃ (SSF-X) (X = 5, 10, 15, 20, and 25 wt %) nanocomposites.

Sample	BET Surface Area
SnS ₂ flowers	41.88 m ² /g
SSF-5 wt %	41.61 m ² /g
SSF-10 wt %	39.41 m ² /g
SSF-15 wt %	42.82 m ² /g
SSF-20 wt %	41.93 m ² /g
SSF-25 wt %	42.47 m ² /g

3.10. PL Measurement

Figure 9, shows the PL spectra of SnS₂-SiO₂@ α -Fe₂O₃ (SSF-X) (X = 10, 15, and 25 wt %) nanocomposites. The broad peak at 600 nm indicates the emission band of SnS₂ flower-like structure. After deposition of various concentrations of SiO₂@ α -Fe₂O₃ nanocomposites on SnS₂, the peak at 600 nm is decreased, indicating the reduction of the recombination rate of electron–hole pairs. The SSF-15 wt % shows minimum intense PL spectra and demonstrates the efficient charge separation

of the composites, as shown in Figure 9. This lower excitonic of PL intensity is due to the stronger capacity of dopants to capture photo-induced electrons, increase the separation rate of photoinduced electrons and holes, and increase photocatalytic activity. Further, a decrease in the light emission intensity indicates the direct radiative recombination and lower recombination of generated carriers. This result shows that a significant reduction in the recombination rate of photogenerated electron–hole pairs is observed in SSF-15 wt % when compared with other nanocomposites. The SSF-15 wt % composite has the lowest full width at half maximum (FWHM) value of 93.23 compared to that of SSF-10 wt % (99.61) and 25 wt % (105.67), respectively. The lowest FWHM value of SSF-15 wt % demonstrated the longer lifetime of the electron–hole pair and thus has the best intrinsic photocatalytic property.

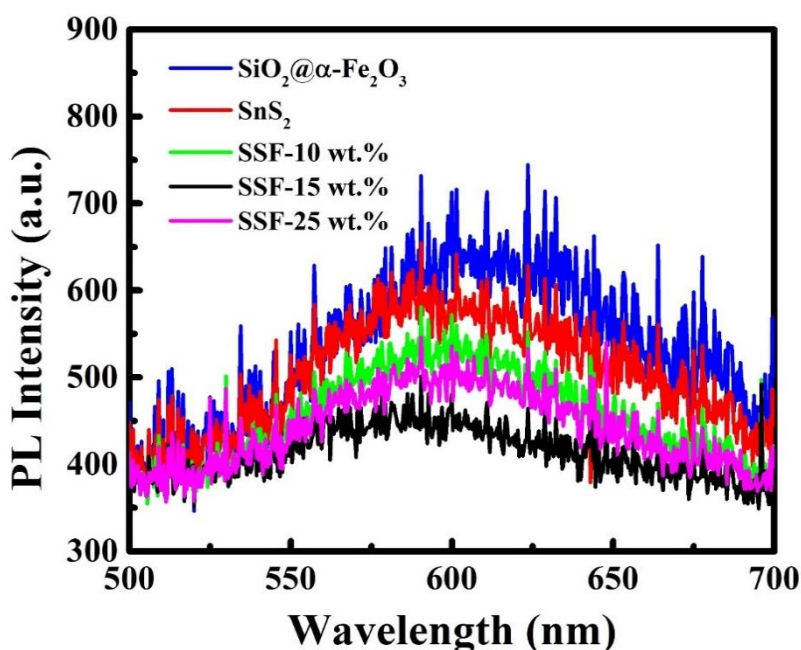


Figure 9. Photoluminescence spectra of $\text{SiO}_2@ \alpha\text{-Fe}_2\text{O}_3$, SnS_2 , and $\text{SnS}_2\text{-SiO}_2@ \alpha\text{-Fe}_2\text{O}_3$ nanocomposites with different weight percentages (SSF-X) (X = 10, 15, and 25 wt %).

3.11. Dye Degradation

Figure 10a,b show the process of MB dye degradation after exposure to visible light irradiation in the presence of SnS_2 and $\text{SnS}_2\text{-SiO}_2@ \alpha\text{-Fe}_2\text{O}_3$ (SSF-15 wt %) photocatalysts. The UV–visible absorption spectrum shows a peak at 664 nm, as was observed for the MB dye in Figure 10a,b. When irradiation time was increased, the absorption intensity of the peak at 664 nm decreased, which confirms the progress of the degradation of the MB dye used as a synthesized photocatalyst. For the 15 wt % $\text{SnS}_2\text{-SiO}_2@ \alpha\text{-Fe}_2\text{O}_3$ sample, complete degradation of the MB dye took only 100 min.

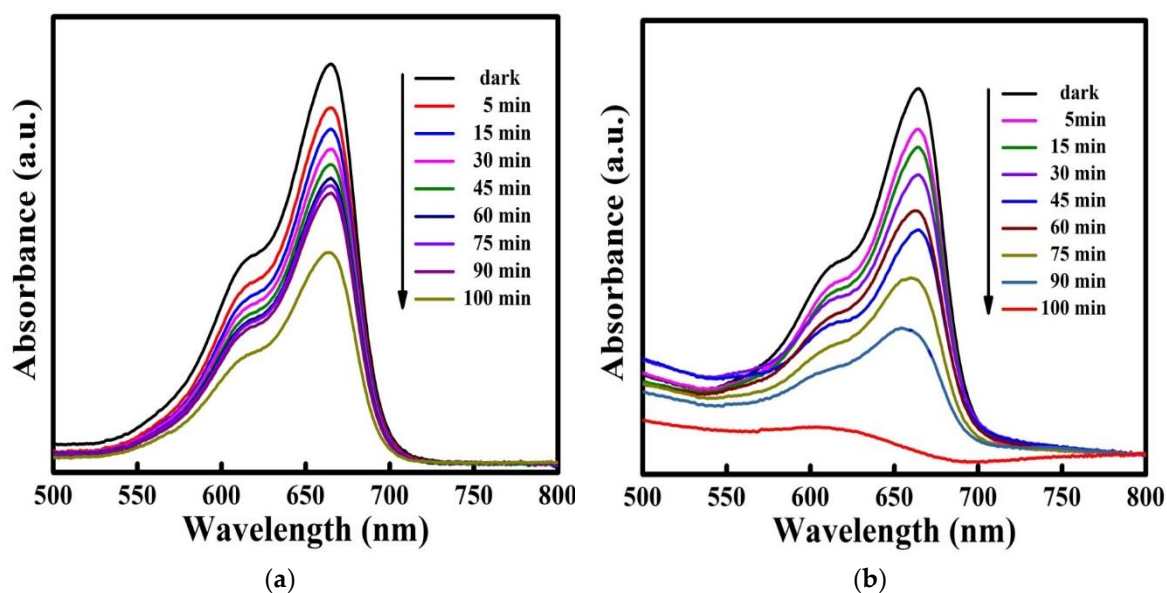


Figure 10. Photodegradation of MB dye in aqueous solution under visible light for (a) SnS_2 and (b) $\text{SnS}_2\text{-SiO}_2@ \alpha\text{-Fe}_2\text{O}_3$ (SSF-15 wt %) nanocomposites.

Furthermore, the photodegradation activities of $\text{SnS}_2\text{-SiO}_2@ \alpha\text{-Fe}_2\text{O}_3$ (SSF-X) with different concentrations of $\text{SiO}_2@ \alpha\text{-Fe}_2\text{O}_3$ were analyzed. The degradation efficiency of SSF catalyst with 5, 10, and 15 wt % $\text{SiO}_2@ \alpha\text{-Fe}_2\text{O}_3$ increased as 47%, 62%, 96%, respectively. Upon increasing the concentration as 20 and 25 wt %, the degradation efficiency was decreased to 58% and 53%, respectively, as shown in Figure 11. It might be due to the accumulation of $\text{SiO}_2@ \alpha\text{-Fe}_2\text{O}_3$ on SnS_2 that reduces the penetration of light into the photocatalyst and generates the larger amount of photon adsorbed on the catalyst surface. Hence, the SSF-15 wt % of the $\text{SiO}_2@ \alpha\text{-Fe}_2\text{O}_3$ is an appropriate amount for the excellent photodegradation of the MB solution.

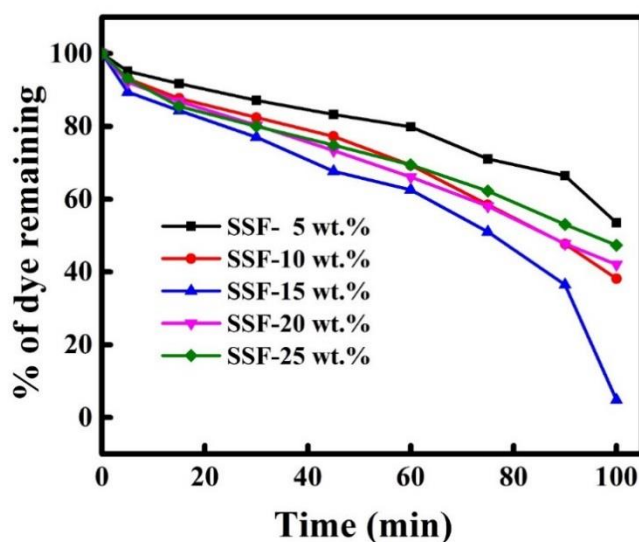


Figure 11. Catalytic activity of different SSF-wt % ($\text{SnS}_2\text{-SiO}_2@ \alpha\text{-Fe}_2\text{O}_3$) nanocomposites on the photodegradation of MB.

Figure 12a shows the percentage of MB dye remaining in the solutions for the SnS_2 , Fe_2O_3 , $\text{SiO}_2@ \alpha\text{-Fe}_2\text{O}_3$, and $\text{SnS}_2\text{-SiO}_2@ \alpha\text{-Fe}_2\text{O}_3$ (SSF-15 wt %) nanocomposites under visible light irradiation.

Dye degradation efficiencies of 19%, 42%, 48%, and 96% were observed for the α -Fe₂O₃, SnS₂, and SiO₂@ α -Fe₂O₃ and SnS₂-SiO₂@ α -Fe₂O₃ (SSF-15 wt %) nanocomposites, respectively, at 100 min. The degradation of phenol (25 ppm) was also carried out in order to evaluate the catalytic activity of the SnS₂-SiO₂@ α -Fe₂O₃ nanocomposite (Figure S3). In the presence of visible-light irradiation, the samples were taken at equal time intervals. The decrease in the distinct peak of phenol at 270 nm indicates the decomposition of phenol. This reveals the effective photocatalytic degradation of phenol done by the SnS₂-SiO₂@ α -Fe₂O₃ nanocomposite. Therefore, the degradation of dye is related to the photocatalytic activity of SnS₂-SiO₂@ α -Fe₂O₃, rather than to the sensitization of dye.

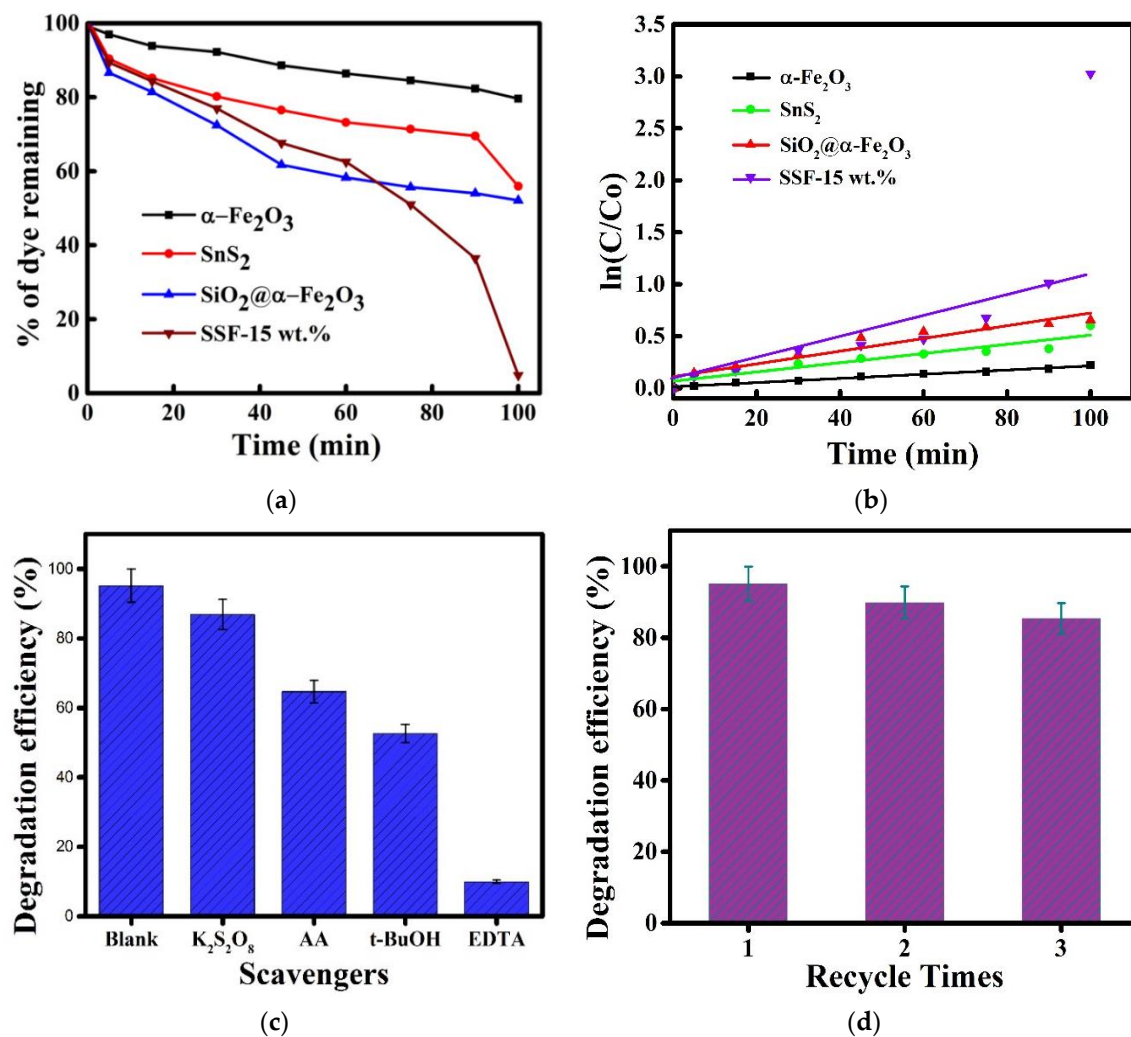


Figure 12. (a) Percentage of degradation and the remaining dye with respect to the different intervals of time (5 to 100 min) in the presence of the photocatalyst α -Fe₂O₃/SnS₂/SiO₂@ α -Fe₂O₃/SnS₂-SiO₂@ α -Fe₂O₃ under irradiation by visible light. (b) Plot of $\ln(C/C_0)$ vs time. (c) Photodegradation efficiency of SSF-15 wt % in the presence of different active-species (scavengers). (d) Reusability of the SSF-15 wt % nanocomposite.

The enhancement of the photocatalytic activity of the SnS₂-SiO₂@ α -Fe₂O₃ (SSF-15 wt %) photocatalyst can be explained by two causes. First, the nanocomposites are prepared by a hydrothermal method having a higher surface area. Secondly, SSF-15 wt % has a very low impedance value in the EIS Nyquist plot. Here, the SiO₂ spheres act as large adsorption sites and good locations for holding the α -Fe₂O₃ nanoparticles and adsorbing the dye molecules. During the photocatalytic reaction, the SnS₂ and α -Fe₂O₃ act as photoactive centers and require a strong interaction between

the dye and the surface of the catalyst for the effective degradation of dye [21,48]. Furthermore, the CB of α -Fe₂O₃ is slightly more negative, while the VB is much more positive than that of SnS₂. This increases the driving force of holes migration when compared to electron transfer. This leads to a decline in the recombination of e⁻/h⁺ pairs, while the charge separation efficiency is increased. Therefore, an efficient charge separation may occur through the strong interfacial interaction in the SnS₂/SiO₂@ α -Fe₂O₃ heterostructures, reducing the photogenerated charge recombination rate and improving the photocatalytic activity. The α -Fe₂O₃ nanoparticles used to trap electrons enhance the photocatalytic activity. Due to the reaction between these trapped electrons and dissolved oxygen in the system, the superoxide radical anions (O₂^{•-}) are formed, which in turn result in the formation of hydroxyl radicals (•OH). These •OH radicals are principally responsible for the oxidation of the organic compounds. This mechanism can be observed in terms of the active surface sites on the catalyst surface and the contact area of the dye and the catalyst. The 15 wt % concentration in SiO₂@ α -Fe₂O₃ nanocomposites increases the number of active sites, which in turn increases the number of hydroxyls (•OH) and superoxide (O₂^{•-}) radicals. Furthermore, degradation efficiency is reduced when the concentration of nanocomposites exceeds the normal range. This may be due to the agglomeration of the nanocomposites, which reduces the penetration of light, as well as the absorbance of the dye and the catalyst.

In Figure 12b, the plot of ln(C/Co) vs time shows that the photocatalytic degradation of MB follows the pseudo-first-order kinetics. The rate constant-k value for the SnS₂-SiO₂@ α -Fe₂O₃ composite is $1.96 \times 10^{-2} \text{ min}^{-1}$, which is about 8, 4, and 3 times greater than that for α -Fe₂O₃ ($2.01 \times 10^{-3} \text{ min}^{-1}$), SnS₂ ($4.43 \times 10^{-3} \text{ min}^{-1}$), and SiO₂@ α -Fe₂O₃ ($6.12 \times 10^{-3} \text{ min}^{-1}$). The sudden increase in rate constant (k) between 90 and 100 min was due to the gradual rise in pH of the reaction medium (7.1–10.3). The oxidation potential, physicochemical, and surface charge properties of the catalyst were affected by the pH of the solution. The alkaline medium favored (i.e., the formation of •OH by the influences of OH⁻ ions on the surface of the catalyst) the decolorization of the dye more than the acidic medium [49,50]. The highest photocatalytic activity was attained with the SSF-15 wt % nanocomposite. Hence, we can prove that the as-synthesized nanocomposite heterostructures enhance the photocatalytic activity. In photocatalytic oxidation reactions, there are several reactive species, such as •OH, O₂^{•-}, holes, and electrons involved in the reaction. To examine the contribution of these species, tertiary butyl alcohol (t-BuOH), potassium persulfate (K₂S₂O₈), acrylamide (AA), and ethylenediaminetetraacetic acid (EDTA) were used as scavenger materials for •OH, electrons, O₂^{•-}, and the holes, respectively, in the reaction process (Figure 12c). The degradation efficiency slightly decreased when the addition of K₂S₂O₈ showed that the electrons play a minimal role in the photocatalytic reaction. The degradation rate of MB further decreased with the addition of AA, indicating reduced involvement of the O₂^{•-} species. The degradation efficiency reduced during the addition of t-BuOH, which shows the partial involvement of •OH. The rate of MB degradation was significantly affected by EDTA, clearly indicating that holes play a major role in the photocatalytic degradation reaction.

To prove the stability and durability of the SnS₂-SiO₂@ α -Fe₂O₃ nanocomposite photocatalyst, the recycle experiments were carried out (Figure 12d). Moreover, the results show that only 9.75% of degradation efficiency was lost during the third cycle, which proves that the SnS₂-SiO₂@ α -Fe₂O₃ nanocomposites possessed higher stability and reusability efficiency (Figure S4).

4. Conclusions

Flower-like SnS₂ and SnS₂-SiO₂@ α -Fe₂O₃ nanocomposites with different weight percentages were successfully synthesized using a simple hydrothermal method. The SSF-15 wt % nanocomposites have higher catalytic activity than other samples. The as-prepared nanocomposites enhanced the amount of adsorption of cationic dye (MB) molecules with the addition of SiO₂@ α -Fe₂O₃ composites on the SnS₂ flowers, thereby increasing the photocatalytic degradation activity. Due to the simplicity of preparation, it is possible to produce a low-cost photocatalyst with higher activity and stability, making it a good

candidate material for applications in environmental purification. Based on our results, it should be noted that $\bullet\text{OH}$, $\text{O}_2^{\bullet-}$, and the holes played a vital role and enhanced the photocatalytic reaction.

Supplementary Materials: The following are available online at <http://www.mdpi.com/1996-1944/11/6/1030/s1>, Figure S1: XRD patterns for SiO_2 and $\text{SiO}_2@ \alpha\text{-Fe}_2\text{O}_3$, Figure S2: Raman spectra of SiO_2 and $\text{SiO}_2@ \alpha\text{-Fe}_2\text{O}_3$, Figure S3: UV-Vis absorbance spectra of phenol in the presence of $\text{SnS}_2\text{-SiO}_2@ \alpha\text{-Fe}_2\text{O}_3$, Figure S4: Comparison of XRD patterns of SSF-15 wt % with the same sample after three cycles.

Author Contributions: T.C.-K.Y. Conceived the idea of experiments, contributed the materials and analysis tools, S.B. and K.U. carried out the preparation and characterization of the samples, S.B. prepared the manuscript, S.B., K.U., G.-T.P., S.K.R and T.C.-K.Y. analyzed and discussed the results of the experiments. All authors have read, commented and approved the final manuscript.

Funding: This research was funded by the ROC Ministry of Science and Technology grant number (MOST 106-2221-E-027-122).

Acknowledgments: The authors would like to thank the Precision Analysis and Research Center, National Taipei University of Technology, Taipei, for its financial support of this research.

Conflicts of Interest: The authors declare no conflict of interest

References

1. Ahmad, A.; Mohd-Setapar, S.H.; Chuong, C.S.; Khatoon, A.; Wani, W.A.; Kumar, R.; Rafatullah, M. Recent advances in new generation dye removal technologies: Novel search for approaches to reprocess wastewater. *RSC Adv.* **2015**, *5*, 30801–30818. [[CrossRef](#)]
2. Gordon, P.F.; Gregory, P. *Organic Chemistry in Colour*; Springer Science & Business Media: Berlin/Heidelberg, Germany, 2012.
3. Ali, I.; Asim, M.; Khan, T.A. Low cost adsorbents for the removal of organic pollutants from wastewater. *J. Environ. Manag.* **2012**, *113*, 170–183. [[CrossRef](#)] [[PubMed](#)]
4. Panizza, M.; Cerisola, G. Removal of organic pollutants from industrial wastewater by electrogenerated Fenton's reagent. *Water Res.* **2001**, *35*, 3987–3992. [[CrossRef](#)]
5. Soltani, N.; Saion, E.; Hussein, M.Z.; Erfani, M.; Abedini, A.; Bahmanrokh, G.; Navasery, M.; Vaziri, P. Visible light-induced degradation of methylene blue in the presence of photocatalytic ZnS and CdS nanoparticles. *Int. J. Mol. Sci.* **2012**, *13*, 12242–12258. [[CrossRef](#)] [[PubMed](#)]
6. Huang, J.; Ren, H.; Liu, X.; Li, X.; Shim, J.-J. Facile synthesis of porous TiO_2 nanospheres and their photocatalytic properties. *Superlattices Microstruct.* **2015**, *81*, 16–25. [[CrossRef](#)]
7. Karimi, L.; Zohoori, S.; Yazdanshenas, M.E. Photocatalytic degradation of azo dyes in aqueous solutions under UV irradiation using nano-strontium titanate as the nanophotocatalyst. *J. Saudi Chem. Soc.* **2014**, *18*, 581–588. [[CrossRef](#)]
8. Habib, M.A.; Ismail, I.M.I.; Mahmood, A.J.; Ullah, M.R. Photocatalytic decolorization of brilliant golden yellow in TiO_2 and ZnO suspensions. *J. Saudi Chem. Soc.* **2012**, *16*, 423–429. [[CrossRef](#)]
9. Huang, Y.; Ding, D.; Zhu, M.; Meng, W.; Huang, Y.; Geng, F.; Li, J.; Lin, J.; Tang, C.; Lei, Z. Facile synthesis of $\alpha\text{-Fe}_2\text{O}_3$ nanodisk with superior photocatalytic performance and mechanism insight. *Sci. Technol. Adv. Mater.* **2015**, *16*, 014801. [[CrossRef](#)] [[PubMed](#)]
10. Chen, C.; Ma, W.; Zhao, J. Semiconductor-mediated photodegradation of pollutants under visible-light irradiation. *Chem. Soc. Rev.* **2010**, *39*, 4206–4219. [[CrossRef](#)] [[PubMed](#)]
11. Ponnusami, V.; Madhuram, R.; Krithika, V.; Srivastava, S.N. Effects of process variables on kinetics of methylene blue sorption onto untreated guava (*Psidium guajava*) leaf powder: Statistical analysis. *Chem. Eng. J.* **2008**, *140*, 609–613. [[CrossRef](#)]
12. Rafatullah, M.; Sulaiman, O.; Hashim, R.; Ahmad, A. Adsorption of methylene blue on low-cost adsorbents: A review. *J. Hazard. Mater.* **2010**, *177*, 70–80. [[CrossRef](#)] [[PubMed](#)]
13. Janani, S.; Sudha Rani, K.S.; Ellappan, P.; Miranda, L.R. Photodegradation of methylene blue using magnetically reduced graphene oxide bismuth oxybromide composite. *J. Environ. Chem. Eng.* **2016**, *4*, 534–541.
14. Li, M.; Qiang, Z.; Pulgarin, C.; Kiwi, J. Accelerated methylene blue (MB) degradation by Fenton reagent exposed to UV or VUV/UV light in an innovative micro photo-reactor. *Appl. Catal. B Environ.* **2016**, *187*, 83–89. [[CrossRef](#)]

15. Barroso, M.; Cowan, A.J.; Pendlebury, S.R.; Grätzel, M.; Klug, D.R.; Durrant, J.R. The role of cobalt phosphate in enhancing the photocatalytic activity of α -Fe₂O₃ toward water oxidation. *J. Am. Chem. Soc.* **2011**, *133*, 14868–14871. [[CrossRef](#)] [[PubMed](#)]
16. Liu, X.; Chen, K.; Shim, J.-J.; Huang, J. Facile synthesis of porous Fe₂O₃ nanorods and their photocatalytic properties. *J. Saudi Chem. Soc.* **2015**, *19*, 479–484. [[CrossRef](#)]
17. Mor, G.K.; Prakasam, H.E.; Varghese, O.K.; Shankar, K.; Grimes, C.A. Vertically oriented Ti–Fe–O nanotube array films: Toward a useful material architecture for solar spectrum water photoelectrolysis. *Nano Lett.* **2007**, *7*, 2356–2364. [[CrossRef](#)] [[PubMed](#)]
18. Klahr, B.; Gimenez, S.; Fabregat-Santiago, F.; Hamann, T.; Bisquert, J. Water oxidation at hematite photoelectrodes: The role of surface states. *J. Am. Chem. Soc.* **2012**, *134*, 4294–4302. [[CrossRef](#)] [[PubMed](#)]
19. Hassena, H. Photocatalytic degradation of methylene blue by using Al₂O₃/Fe₂O₃ nano composite under visible light. *Mod. Chem. Appl.* **2016**. [[CrossRef](#)]
20. Pal, B.; Sharon, M.; Nogami, G. Preparation and characterization of TiO₂/Fe₂O₃ binary mixed oxides and its photocatalytic properties. *Mater. Chem. Phys.* **1999**, *59*, 254–261. [[CrossRef](#)]
21. Zhang, Y.C.; Du, Z.N.; Li, K.W.; Zhang, M.; Dionysiou, D.D. High-performance visible-light-driven SnS₂/SnO₂ nanocomposite photocatalyst prepared via in situ hydrothermal oxidation of SnS₂ nanoparticles. *ACS Appl. Mater. Interfaces* **2011**, *3*, 1528–1537. [[CrossRef](#)] [[PubMed](#)]
22. Yao, K.; Li, J.; Shan, S.; Jia, Q. One-step synthesis of urchinlike SnS/SnS₂ heterostructures with superior visible-light photocatalytic performance. *Catal. Commun.* **2017**, *101*, 51–56. [[CrossRef](#)]
23. Burton, L.A.; Colombara, D.; Abellon, R.D.; Grozema, F.C.; Peter, L.M.; Savenije, T.J.; Dennler, G.; Walsh, A. Synthesis, characterization, and electronic structure of single-crystal SnS, Sn₂S₃, and SnS₂. *Chem. Mater.* **2013**, *25*, 4908–4916. [[CrossRef](#)]
24. Chaudhuri, T.K.; Tiwari, D. Earth-abundant non-toxic Cu₂ZnSnS₄ thin films by direct liquid coating from metal–thiourea precursor solution. *Sol. Energy Mater. Sol. Cells* **2012**, *101*, 46–50. [[CrossRef](#)]
25. Yang, H.; Jauregui, L.A.; Zhang, G.; Chen, Y.P.; Wu, Y. Nontoxic and abundant copper zinc tin sulfide nanocrystals for potential high-temperature thermoelectric energy harvesting. *Nano Lett.* **2012**, *12*, 540–545. [[CrossRef](#)] [[PubMed](#)]
26. An, X.; Jimmy, C.Y.; Tang, J. Biomolecule-assisted fabrication of copper doped SnS₂ nanosheet–reduced graphene oxide junctions with enhanced visible-light photocatalytic activity. *J. Mater. Chem. A* **2014**, *2*, 1000–1005. [[CrossRef](#)]
27. Lei, Y.; Song, S.; Fan, W.; Xing, Y.; Zhang, H. Facile synthesis and assemblies of flowerlike SnS₂ and In³⁺-doped SnS₂: Hierarchical structures and their enhanced photocatalytic property. *J. Phys. Chem. C* **2009**, *113*, 1280–1285. [[CrossRef](#)]
28. Anderson, C.; Bard, A.J. Improved photocatalytic activity and characterization of mixed TiO₂/SiO₂ and TiO₂/Al₂O₃ materials. *J. Phys. Chem. B* **1997**, *101*, 2611–2616. [[CrossRef](#)]
29. Zou, L.; Luo, Y.; Hooper, M.; Hu, E. Removal of VOCs by photocatalysis process using adsorption enhanced TiO₂–SiO₂ catalyst. *Chem. Eng. Process. Process Intensif.* **2006**, *45*, 959–964. [[CrossRef](#)]
30. Tang, W.; Su, Y.; Wang, X.; Li, Q.; Gao, S.; Shang, J.K. Synthesis of a superparamagnetic MFNs@SiO₂@Ag₄SiW₁₂O₄₀/Ag composite photocatalyst, its superior photocatalytic performance under visible light illumination, and its easy magnetic separation. *RSC Adv.* **2014**, *4*, 30090–30099. [[CrossRef](#)]
31. Fu, Y.Y.; Yang, C.X.; Yan, X.P. Fabrication of ZIF-8@SiO₂ Core–Shell Microspheres as the Stationary Phase for High-Performance Liquid Chromatography. *Chem. Eur. J.* **2013**, *19*, 13484–13491. [[CrossRef](#)] [[PubMed](#)]
32. Wu, H.-S.; Sun, L.-D.; Zhou, H.-P.; Yan, C.-H. Novel TiO₂–Pt@SiO₂ nanocomposites with high photocatalytic activity. *Nanoscale* **2012**, *4*, 3242–3247. [[CrossRef](#)] [[PubMed](#)]
33. Zhu, S.-R.; Qi, Q.; Zhao, W.-N.; Wu, M.-K.; Fang, Y.; Tao, K.; Yi, F.-Y.; Han, L. Hierarchical core–shell SiO₂@PDA@BiOBr microspheres with enhanced visible-light-driven photocatalytic performance. *Dalton Trans.* **2017**, *46*, 11451–11458. [[CrossRef](#)] [[PubMed](#)]
34. Tatsuo, K.; Yusuke, Y.; Nobuyoshi, M. Highly Photoactive Porous Anatase Films Obtained by Deformation of 3D Mesostructures. *Chem. Eur. J.* **2011**, *17*, 4005–4011.
35. Hamid, O.; Simin, R.; Xiangfen, J.; Yoshihiro, N.; Ali, B.; Soichi, W.; Yusuke, Y. Unusual Antibacterial Property of Mesoporous Titania Films: Drastic Improvement by Controlling Surface Area and Crystallinity. *Chem. Asian J.* **2010**, *5*, 1978–1983.

36. Zhang, W.; Fröba, M.; Wang, J.; Tanev, P.T.; Wong, J.; Pinnavaia, T.J. Mesoporous Titanosilicate Molecular Sieves Prepared at Ambient Temperature by Electrostatic (S+I-, S+X-I+) and Neutral (S°I°) Assembly Pathways: A Comparison of Physical Properties and Catalytic Activity for Peroxide Oxidations. *J. Am. Chem. Soc.* **1996**, *118*, 9164–9171. [[CrossRef](#)]
37. Xiong, Y.; Xu, W.; Ding, D.; Lu, W.; Zhu, L.; Zhu, Z.; Wang, Y.; Xue, Q. Ultra-sensitive NH₃ sensor based on flower-shaped SnS₂ nanostructures with sub-ppm detection ability. *J. Hazard. Mater.* **2018**, *341*, 159–167. [[CrossRef](#)] [[PubMed](#)]
38. Uma, K.; Arjun, N.; Pan, G.-T.; Yang, T.C.-K. The photodeposition of surface plasmon Ag metal on SiO₂@ α -Fe₂O₃ nanocomposites sphere for enhancement of the photo-Fenton behavior. *Appl. Surf. Sci.* **2017**, *425*, 377–383. [[CrossRef](#)]
39. Wei, R.; Zhou, T.; Hu, J.; Li, J. Glutathione modified ultrathin SnS₂ nanosheets with highly photocatalytic activity for wastewater treatment. *Mater. Res. Express* **2014**, *1*, 025018. [[CrossRef](#)]
40. Liu, J.; Jing, L.; Gao, G.; Xu, Y.; Xie, M.; Huang, L.; Ji, H.; Xie, J.; Li, H. Ag₂S quantum dots in situ coupled to hexagonal SnS₂ with enhanced photocatalytic activity for MO and Cr (vi) removal. *RSC Adv.* **2017**, *7*, 46823–46831. [[CrossRef](#)]
41. Smart, R.S.C.; Skinner, W.M.; Gerson, A.R. XPS of sulphide mineral surfaces: Metal-deficient, polysulphides, defects and elemental sulphur. *Surf. Interface Anal.* **1999**, *28*, 101–105. [[CrossRef](#)]
42. Merino, N.A.; Barbero, B.P.; Eloy, P.; Cadús, L.E. La_{1-x}Ca_xCoO₃ perovskite-type oxides: Identification of the surface oxygen species by XPS. *Appl. Surf. Sci.* **2006**, *253*, 1489–1493. [[CrossRef](#)]
43. Grosvenor, A.; Kobe, B.; Biesinger, M.; McIntyre, N. Investigation of multiplet splitting of Fe 2p XPS spectra and bonding in iron compounds. *Surf. Interface Anal.* **2004**, *36*, 1564–1574. [[CrossRef](#)]
44. Yamashita, T.; Hayes, P. Analysis of XPS spectra of Fe²⁺ and Fe³⁺ ions in oxide materials. *Appl. Surf. Sci.* **2008**, *254*, 2441–2449. [[CrossRef](#)]
45. Mitchell, D.; Clark, K.; Bardwell, J.; Lennard, W.; Massoumi, G.; Mitchell, I. Film thickness measurements of SiO₂ by XPS. *Surf. Interface Anal.* **1994**, *21*, 44–50. [[CrossRef](#)]
46. Huang, Y.; Sutter, E.; Sadowski, J.T.; Cotlet, M.; Monti, O.L.; Racke, D.A.; Neupane, M.R.; Wickramaratne, D.; Lake, R.K.; Parkinson, B.A. Tin Disulfide—An Emerging Layered Metal Dichalcogenide Semiconductor: Materials Properties and Device Characteristics. *ACS Nano* **2014**, *8*, 10743–10755. [[CrossRef](#)] [[PubMed](#)]
47. He, M.; Yuan, L.-X.; Huang, Y.-H. Acetylene black incorporated three-dimensional porous SnS₂ nanoflowers with high performance for lithium storage. *RSC Adv.* **2013**, *3*, 3374–3383. [[CrossRef](#)]
48. Pawar, R.C.; Kang, S.; Park, J.H.; Kim, J.-H.; Ahn, S.; Lee, C.S. Evaluation of a multi-dimensional hybrid photocatalyst for enrichment of H₂ evolution and elimination of dye/non-dye pollutants. *Catal. Sci. Technol.* **2017**, *7*, 2579–2590. [[CrossRef](#)]
49. Sanatgar-Delshade, E.; Habibi-Yangjeh, A.; Khodadadi-Moghaddam, M. Hydrothermal low-temperature preparation and characterization of ZnO nanoparticles supported on natural zeolite as a highly efficient photocatalyst. *Monatshfte Chem. Chem. Mon.* **2011**, *142*, 119–129. [[CrossRef](#)]
50. Shanthi, M.; Kuzhalosai, V. *Photocatalytic Degradation of an azo dye, Acid Red 27, in Aqueous Solution Using Nano ZnO*; NISCAIR-CSIR: New Delhi, India, 2012.

